Theses and Dissertations

2005-02-23

Optical Detection of Ultracold Neutral Calcium Plasmas

Elizabeth Ann Cummings
Brigham Young University - Provo

OPTICAL DETECTION OF

ULTRACOLD NEUTRAL

CALCIUM PLASMAS

by

Elizabeth Ann Cummings

A thesis submitted to the faculty of

Brigham Young University

in partial fulfillment of the requirements for the degree of

Master of Science

Department of Physics and Astronomy

Brigham Young University

April 2005

BRIGHAM YOUNG UNIVERSITY

GRADUATE COMMITTEE APPROVAL

of a thesis submitted by

Elizabeth Ann Cummings

This thesis has been read by each member of the following graduate committee and by majority vote has been found to be satisfactory.

_____	_____
Date	Scott D. Bergeson, Chair
_____	_____
Date	Dallin S. Durfee
_____	_____
Date	Grant W. Mason

BRIGHAM YOUNG UNIVERSITY

As chair of the candidate's graduate committee, I have read the thesis of Elizabeth Ann Cummings in its final form and have found that (1) its format, citations, and bibliographical style are consistent and acceptable and fulfill university and department style requirements; (2) its illustrative materials including figures, tables, and charts are in place; and (3) the final manuscript is satisfactory to the graduate committee and is ready for submission to the university library.

_____   _____
Date   Scott D. Bergeson
                                                                           Chair, Graduate Committee

Accepted for the Department

                                                                 _____
                                                                 Ross L. Spencer
                                                                 Graduate Coordinator

Accepted for the College

                                                                 _____
                                                                 Earl M. Woolley, Dean
                                                                 College of Physical and Mathematical Sciences

ABSTRACT

OPTICAL DETECTION OF ULTRACOLD NEUTRAL CALCIUM PLASMAS

Elizabeth Ann Cummings

Department of Physics and Astronomy

Master of Science

We demonstrate an optical method to detect calcium ions in an ultracold plasma. We probe the plasma with a 397 nm laser beam tuned to the Ca II $^2S_{1/2}$ to $^2P_{1/2}$ transition. The probe laser beam is focused to a 160 μm waist allowing fine spatial resolution. Ions are detected by measuring fluorescence using a Photo-Multiplier Tube (PMT). The signal, an average of 4000 acquisitions, has a temporal resolution of 120 ns. We present the details of this method, potential improvements, and prospects of imaging the expanding plasma ions. We also present preliminary work on spatially resolved absorption measurements, as well as additional studies.

Contents

List of Figures

Chapter 1

Introduction

Ultracold plasmas are a unique species of plasma, occupying a rare position in phase-space. Their initial densities and temperatures, around a few milliKelvin, easily distinguish them from other plasmas. Ultracold plasmas bridge the traditional boundaries of atomic physics and plasma physics, as well as between atomic physics and condensed matter (many-body) physics.

Understanding the dynamics of ultracold plasmas will contribute information about other plasma systems. The dynamics of ultracold plasmas are most similar to strongly coupled plasmas, because the nearest neighbor coulomb energy is larger than any other relevant energy. Because of the potential for strong coupling, studies on these multi-component ultracold plasmas at milliKelvin temperatures may contribute to understanding high temperature, high density plasmas, such as the surfaces of neutron stars, the interiors of gaseous planets, and laser-produced fusion plasmas.

Ultracold plasmas have been studied using several detection methods, such as counting ions and electrons using particle detectors, probing the electron density using radio frequency electric fields, and ion absorption imaging. Each detection

method has its limitations and strengths, and has contributed to our understanding of the system dynamics.

1.1 Previous Studies of Ultracold Plasmas

The first ultracold plasma studies were published in 1999[1]. In these studies xenon atoms were first cooled to 10 μK in a Magneto-Optical Trap (MOT) (see Sec. 2.1). The plasma was created by photoionizing the xenon using a pulsed laser beam 10 ns in duration. After ionization the electron temperatures were usually $T_e = 100$ K and xenon ion temperatures were $T_i = 1$ mK, due to recoil. The initial electron temperature is controlled by the wavelength of the ionization pulse. The ionization pulse energy also determines the number of ions created.

The ions were detected using a microchannel plate and electrons were detected using a single channel electron multiplier (channeltron). It was determined from these measurements that hot electrons escape from the cloud quickly t$\sim 1\mu$s. Residual warm electrons in the cloud quickly rethermilize due to collisions and a small fraction gain enough energy to also escape. The resulting charge imbalance creates a Coulomb well that, if deep enough, can trap the remaining electrons. Typically 90-99% of the electrons were trapped in the Coulomb well of the xenon plasma [2], depending on the initial density.

Ions and electrons in a plasma can recombine to form a neutral atom. Recombination occurs through two mechanisms: radiative and three-body. In radiative recombination an electron collides with an ion and binds to an atomic state. The surplus energy is emitted as a photon. In Three-Body Recombination (TBR) two

2

free electrons collide with an ion. One electron binds to the ion and the surplus momentum is carried away by the other electron. The TBR rate, $R^{(3)}$, per xenon ion for a known electron density, n_e, and plasma electron temperature, T_e, is [9]

$$R^{(3)} = 3.9 \times 10^{-9} \frac{K^{-9/2}}{(cm^{-3})^2} s^{-1} \frac{[n_e(cm^{-3})]^2}{[T_e(K)]^{9/2}}. \tag{1.1}$$

TBR occurs more rapidly than radiative recombination when the electron density is high and the plasma electron temperature is low, making TBR the dominant form of recombination in an ultracold plasma.

It was indirectly observed [2] that the three-body recombination lifetime for xenon plasma was 100 μs long. However, a simple application of TBR the (1.1) predicted a recombination lifetime of 1 ns. To explain this discrepancy it was conjectured that TBR theory broke down at low electron temperatures due to electron strong coupling. Electron strong coupling occurs when the electron kinetic energy E_e is much less than the electron-electron Coulomb interaction. This is represented by the Coulomb coupling parameter Γ_e,

$$\Gamma_e = \frac{e^2}{4\pi\epsilon_o a} \frac{1}{k_b T_e}, \tag{1.2}$$

where $a = (\frac{4\pi}{3} n_e)^{-1/3}$, e is the elemental charge, and ϵ_o electric permittivity constant. For strong coupling $\Gamma_e \geq 1$. It was suggested in [1] that both the ions and electrons were strongly coupled. We now know that this is incorrect [7, 8, 9, 10, 11].

1.1.1   Exciting Plasma Oscillations using Radio Frequency Electric Fields

In the second xenon plasma study plasma oscillations were excited by applying a Radio Frequency (RF) electric field across the plasma. The plasma absorbs energy when the applied RF frequency matches the plasma frequency. The RF field then acts as a driving force on the resonant electrons. As electrons gain kinetic energy they overcome the Coulomb potential, leave the plasma cloud, and are measured by the channeltron. The plasma frequency, f_e, corresponds to the electron density, n_e,

$$f_e = \frac{1}{2\pi}\sqrt{\frac{e^2 n_e}{\epsilon_o m_e}}, \tag{1.3}$$

where m_e is the electron mass. By measuring the electron counts as a function of time for a variety of RF frequencies, the average plasma density can be mapped out (Fig. 1.1).

Figure 1.1(a) shows the electron signal with and without an applied RF field. In both cases the large first peak is from hot electrons escaping the plasma soon after formation. As they leave a Coulomb potential forms, trapping cooler electrons. In case (a) a DC electric field is applied to extract the trapped electrons, generating the broad peak at 25 μs. When a 5 MHz RF field is applied, the trapped electrons escape when the plasma frequency matches the RF frequency (dotted line). Figure 1.1(b) shows several of these trapped electron peaks for different RF frequencies. It shows the average plasma density as a function of time, from which the plasma expansion velocity is extracted (see Fig. 1.2).

The ion expansion velocities for different initial electron temperatures are
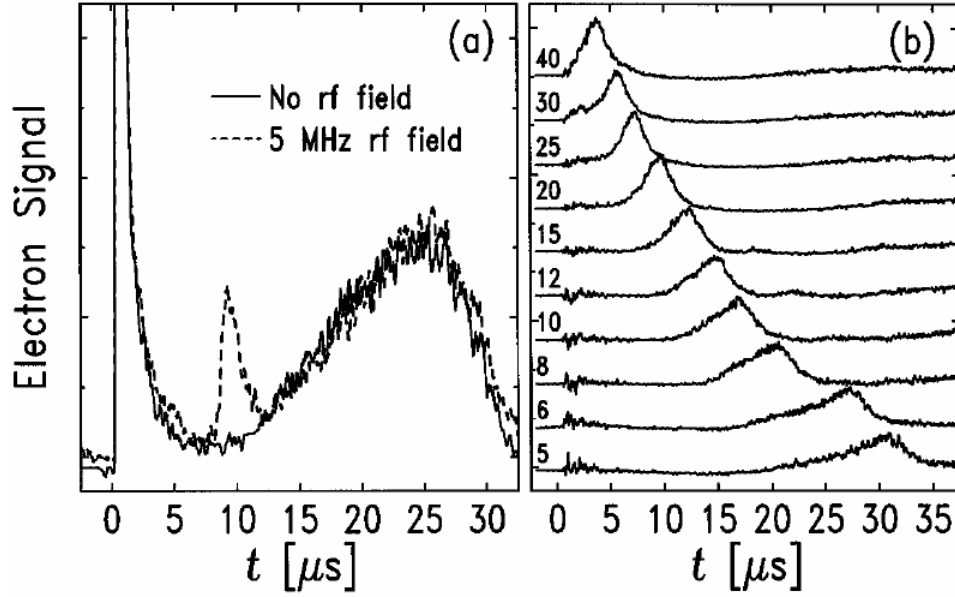
4

Figure 1.1: RF Oscillations in Xenon Plasma[2]. Fig. (a) 2nd Peak, no RF field: a DC electric field extracts trapped plasma electrons. 5 MHz RF field: RF field drives resonant electrons causing a peak. Fig. (b) Electron signal for several RF frequencies (offset for clarity).

shown in Fig. 1.2. For $E_e > 70$K the ion expansion velocity depends on the electron temperature, as expected. However, for $E_e < 70$K, the expansion velocity is independent of the electron temperature. This expansion data was first compared to a hydrodynamic model for two cases: $E_e < 70$K and $E_e > 70$K [2].

In the $E_e > 70$K case the expansion is driven by the pressure of the electron gas. This implies that the ions acquire a velocity of order $\sqrt{\frac{k_b T_e}{m_i}}$. The model suggests that 90% of the initial kinetic energy of the electrons is transferred to the ion's kinetic energy. However, this calculation neglected the thermodynamics of the expanding
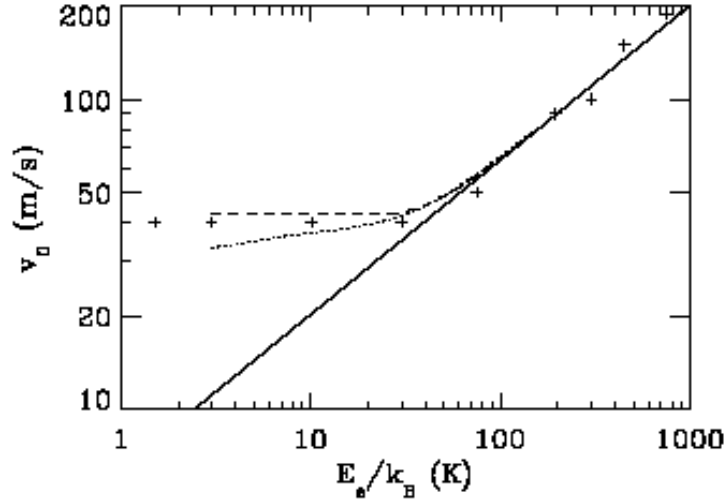
www.manaraa.com

Figure 1.2: Expanding Plasma Velocity at Various Initial Electron Temperatures: +
are the data points taken in [2]. Solid line is a hydrodynamic fit [2]. Dotted line is a
TBR fit by [8]. Dashed line considers TBR and electron-Rydberg collisions [8].

trap. As the electrons move they perform work on the ions, causing the electrons

to cool adiabatically. The thermodynamics were later considered in two theoretical

papers [8, 9].

For $E_e < 70$ K the electrons expand faster than expected and do not follow the

hydrodynamic model. This corresponds to the case $\Gamma_e \sim 1$, suggesting that electron

correlations influence the expansion dynamics. However, more thorough studies of

the system [8, 9, 10, 11], have concluded that the asymptotic velocity is not caused

by strong coupling. Rather, TBR causes thermal heating of the electron gas and

preferentially removes slow ions from the plasma. Concurrently, as electron-electron

correlations begin to develop, the correlation energy heats the electrons, raising the

electron temperature, and keeping Γ_e below unity. This transfer of correlation energy

to kinetic energy is referred to as correlation or disorder-induced heating. It occurs on a time scale proportional to the inverse plasma oscillation frequency.

The ion expansion velocity calculated by Robicheaux [8] is shown in Fig. 1.2. The best fit (dashed line) is when TBR and electron-Rydberg scattering are both considered. Thus the asymptotic expansion velocity reported in [2] is explained by TBR and electron-Rydberg atom collisions rather than strong electron coupling.

TBR and electron-Rydberg collisions were validated as the physical process of the expanding plasma in a recent paper [12]. The electron temperature measurements coincided with Robicheaux's calculations [8]. It was found that $\Gamma_e < 0.5$, as predicted in theory [8, 12].

1.1.2   Limitations of RF Detection

TBR and electron-Rydberg collisions do not fully describe ultracold plasma dynamics. RF electron detection only measures average plasma characteristics, resulting in poor temporal resolution and no spatial resolution. Temporal resolution is poor because the signal depends on the plasma response to an RF field, which lasts a few microseconds. Additionally, a thorough examination of the plasma RF response [20] found no normal or discrete modes. Rather, the response is dominated by a continuous quasimode. As a result, the plasma is driven by the RF field before the plasma frequency equals the RF frequency, producing an early plasma response. Thus, the measured average plasma density underestimates the actual peak density by about a factor of 3 [20].

Other detection methods must be used to better determine the plasma dynamics, particularly at times soon after plasma formation ($< 1\mu s$). The plasma dynamics

soon after it is formed (< 200ns) are vastly different from when it is expanding. Dynamics of the newly formed plasma, can only be measured using another detection method with spatial and better time resolution.

1.2 Spatial Considerations of the Plasma Expansion

A simulation of the xenon plasma expansion [8] calculated the acceleration for three initial electron temperatures 15K, 30K, and 75K (see Fig. 1.3). The radial acceleration, $a(r)$, was scaled by the ion mass, M_i, electron temperature, T_e, and average
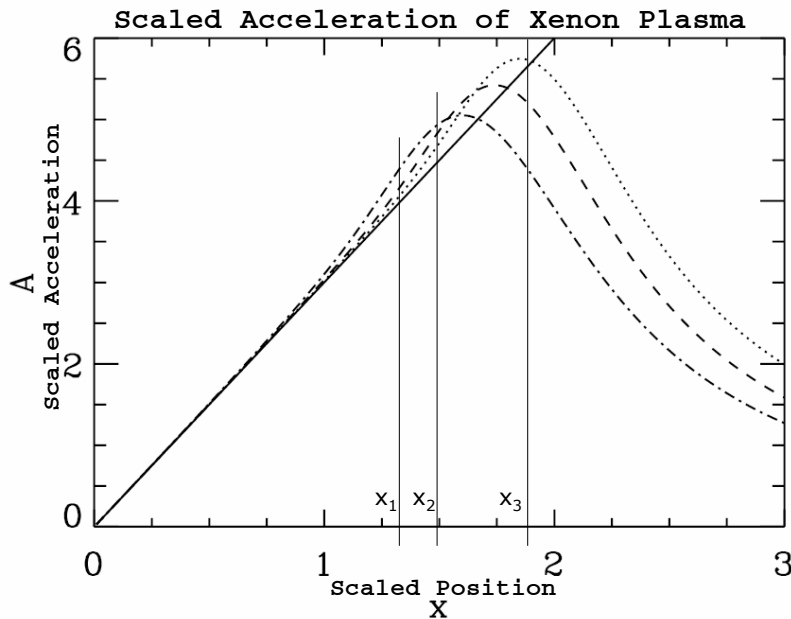

Figure 1.3: Xe plasma scaled acceleration vs. scaled radial distance [8] for electron temp.: 15K (dotted), 30K (dash), and 75K (dot-dash).

8

distance, $\sqrt{<r^2>}$. The scaled acceleration A was

$$A = \frac{a(r)M_i\sqrt{<r^2>}}{k_bT_e},\qquad(1.4)$$

and the scaled radial distance from the plasma center was $x = \frac{r}{\sqrt{<r^2>}}$. We see from figure 1.3, ions with $x \le 1.5 = x_2$ experience an approximately linear outward acceleration, independent of temperature. The solid line depicts an extended linear acceleration in r. Such an acceleration gives a velocity linear in r, preserving the Gaussian spatial distribution throughout the expansion.
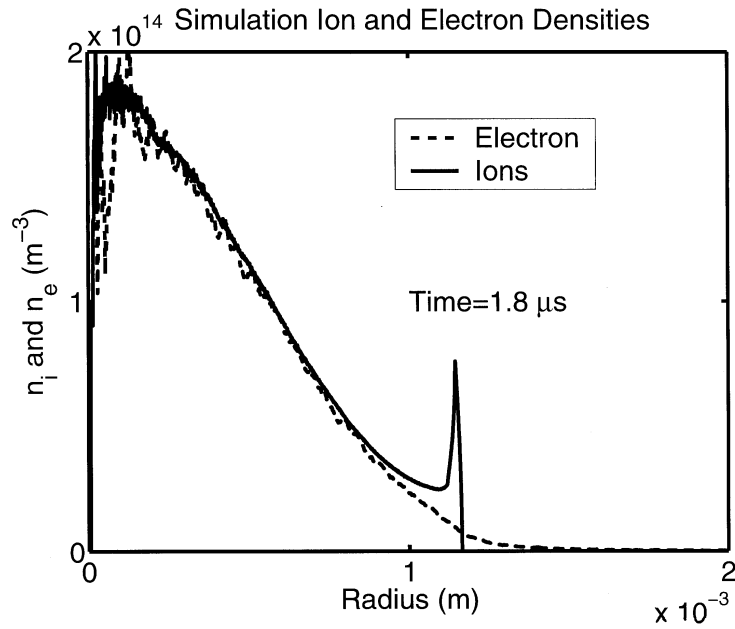

Figure 1.4: A numerical simulation of the expanding calcium plasma [14]. A shock wave develops due to non-linear acceleration at the plasma edge.

However, the region beyond x_2 accelerates non-linearly with x, and the initial Gaussian spatial distribution is not preserved. Instead a distinctive build up of ions occurs. In Fig. 1.3 for $T_e = 75K$ (dot-dashed line), the acceleration, A', is the same for x_1 and x_3. Particles between x_1 and x_3 have an acceleration greater than A'. As the plasma expands, particles in this region can potentially catch up to those initially at x_3. This was predicted in a simulation [14], the results are shown in Fig. 1.4. The figure shows that the plasma expansion for $x \leq x_2$ retains the initial Gaussian distribution, while the plasma edge clumps together into an outer ring, or shockwave.

1.3   Absorptive Imaging

The Killian group at Rice University [4, 5, 6, 7] used an absorptive imaging technique to study strontium ultracold plasmas. They imaged their plasma using a CCD camera and a probe laser beam tuned to an atomic transition in the strontium ion. This was the first published spatial and temporal measurement of the plasma ions (see Fig.1.5). They had a signal-to-noise ratio of 5:1, a temporal resolution of 50 ns, and a spatial resolution of 100 μm.

Killian has discovered that soon after the plasma develops strong coupling is achieved between ions. For several hundred nanoseconds, the coupling is sustained with $\Gamma_i \sim 2$. This suggests that disorder-induced heating, which lasts about 100 ns for strontium, leads to equilibrium just barely within the strongly coupled regime. Additionally, there is no strong coupling for electrons since $\Gamma_e \sim 0.3$. With no electron strong coupling the electron temperature can be calculated directly from the ion acceleration.

10
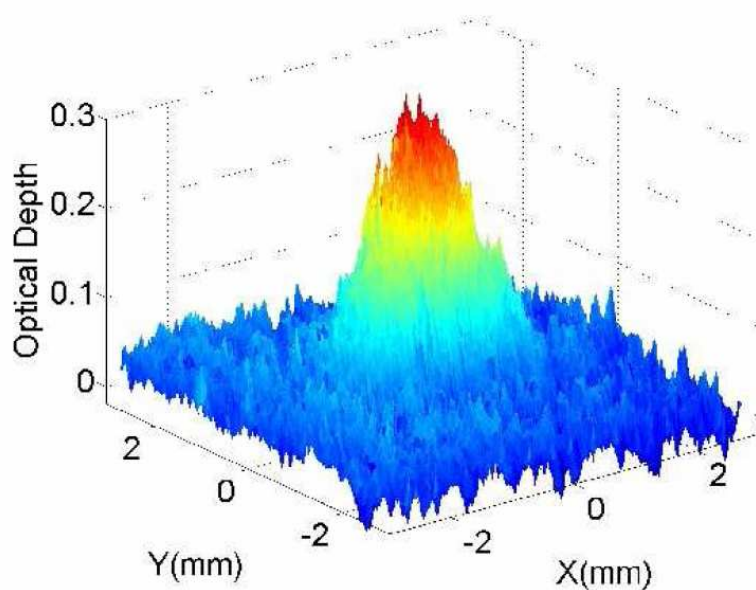
Figure 1.5: Absorptive Imaging of Strontium (Sr) [7]. Sr ions in an ultracold plasma absorb a probe beam. The beam is measured by a CCD camera.

Table 1.1 is a time summary of calcium plasma dynamics for T_e= 100 K. It clearly shows that the plasma changes dramatically in the first microsecond, emphasizing the importance of high temporal resolution. The table details are conclusions drawn from papers previously cited in this chapter. The time has been adjusted for a calcium mass.

1.4   Motivation for Further Studies

There is great need to study ultracold plasmas under low noise, and high temporal and spatial resolution. Killian's work is a substantial improvement from the RF

11

Table 1.1: Calcium Plasma Dynamics

Time (ns)	Calcium Plasma Dynamics for T_e= 100 K
$t < 0$	MOT spherical cloud of essentially stationary atoms
t=0	Plasma created by a 10 ns laser pulse
t $\sim$ 24	Hottest electrons have promptly left the plasma [1]
	Prompt losses end when sufficient space charge builds up to trap electons.
t $\sim$ 68	Ion-Ion coupling breaks down as disorder-induced heating ends.[7]
t $\sim$ 71	Electrons thermalize [8]
t $\geq$ 71	Plasma Expands [1]
	As plasma expands TBR and electron-Rydberg scattering occur.
t $= 1.8\mu$s	Shock wave develops [14]
t $\sim$ 1 μs	Electrons and Ions thermalize [7]

detection of xenon plasma electrons. However, greater signal-to-noise ratios and finer time resolution will make it possible to measure a shock wave of the expanding plasma and other plasma dynamics.

There are currently no published time dependent measurements of electron temperatures. There are also no direct measurements of electron density or electron-ion recombination. There are ion density measurements for strontium, detected by absorptive imaging. From these measurements the ion temperature and ion-ion and electron-electron coupling parameters have been calculated.

We have set out to measure the time evolution of the ion density profile and ion number in ultracold calcium plasmas as a function of initial ion density and electron temperature. By determining the number and density of ions in our trap we will know how the plasma expands and evolves in time. Our method should have high temporal resolution and good signal-to-noise so that we can resolve the plasma shockwave.

Chapter 2

Plasma Formation, Expansion, and Detection

2.1   Creating an Ultracold Calcium Plasma

To make an ultracold plasma we utilize several tools of atomic physics. A beam of hot calcium atoms (625°C) enters a vacuum chamber and is cooled and trapped in a MOT [13]. The MOT (Fig. 2.1) consists of a pair of anti-Helmholz coils and six laser beams at 423 nm which are slightly detuned below the Ca $^1S_0 \rightarrow {}^1P_1$ resonance. The coils create a magnetic field gradient and are arranged in anti-Helmholtz configuration so the magnetic field is zero at the trap center.

As the atoms move toward the magnetic coils, the energies of the $^1P_1$ m=+1,0,-1 sub-levels change via the Zeeman shift. Additionally, atoms experience a Doppler shift as they move toward the laser beams. The laser is below resonance for atoms moving toward the trap and in resonance for atoms moving away from the trap. These atoms are 'pushed' toward the trap by the laser. This 'pushing' is actually the atom recoiling after it absorbs a photon. This happens thousands of times until the atom is cooled and trapped in the MOT at 2 mK.

It takes about 30 ms for the MOT to load. Typically our MOT traps 5×10^9
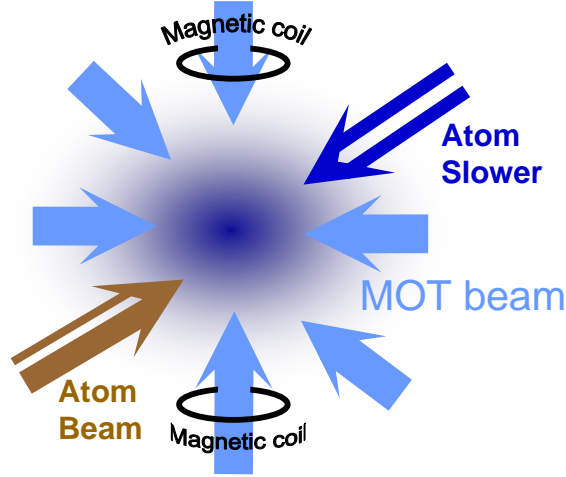
Figure 2.1: Magneto-Optical Trap (MOT). The MOT includes 6 laser beams at 423 nm and the magnetic coils. The coils create a magnetic field that is zero at the trap center.

atoms/cm^3. It is spherical with a 3.2 mm diameter, and has a total population of 1×10^7 atoms.

Once the calcium is trapped, the MOT is turned off and the atoms are photoionized by a 3 ns laser pulse at 390 nm, creating a neutral plasma (see Fig. 2.2). The initial electron temperature is determined by the photon energy in the laser pulse:

$$T_e = (E_{photon} - E_{ionize})/k_B \geq 0.1K \tag{2.1}$$

The photoionization pulse is generated from a tunable dye laser, pumped by a 355 nm Nd:YAG pulsed laser. The tunablity of the dye laser allows easy adjustment of the pulse wavelength, which corresponds to the electron temperature.
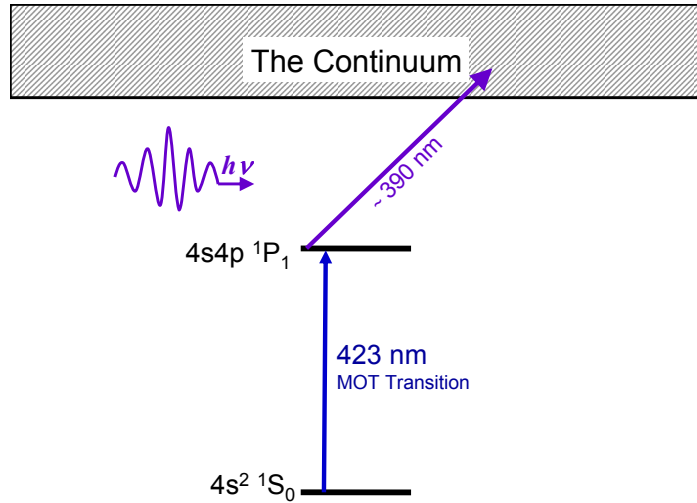
14

Figure 2.2: Calcium Energy Level Scheme. Calcium is confined in the MOT with a $\lambda = 423$ nm laser. $^1P_1$ state atoms are ionized by a laser pulse above the ionization energy (> 390 nm), creating a plasma.

2.2 Detecting Plasma Ions

Our goal is to image our plasma in order to measure the ion density, the ion number, and ion temperature. This requires good spatial ($< 100\mu$m) and temporal resolution. If we want to resolve a shock wave we need a good signal-to-noise ratio.

We developed two ion detection methods: optical absorption and ion fluorescence measurements. I will describe both of these methods. The fluorescence measurements have been, by far, the most successful.

2.2.1 Optical Absorption Detection

Optical absorption detection is similar to absorption imaging. However, we measure the ion absorption of a *focused* probe beam in the plasma (see Fig. 2.3). The probe
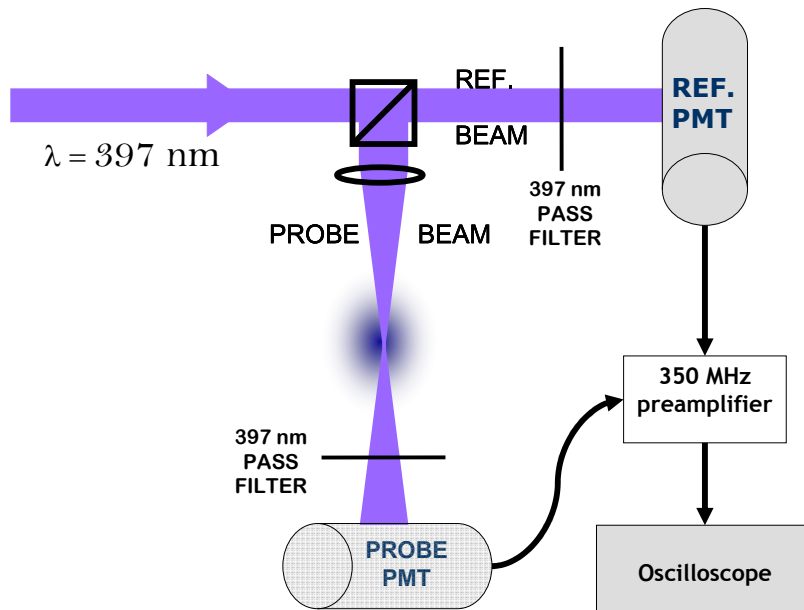
Figure 2.3: Optical detection of calcium ions by absorption measurement. A laser beam in resonance with the ion transition is split into two equal beams at the beam splitter. The probe beam is absorbed by the plasma ions and the reference beam measures noise.

beam is focused to 160 μm spot, absorbed by plasma ions, and measured by a Photo-Multiplier Tube (PMT). An additional reference PMT measures beam fluctuations and pick-up noise. Both PMTs have a 397 nm narrowband-pass filter to block out room light and MOT fluorescence. We remove laser intensity fluctuations by dividing the signal PMT by the reference PMT. The two PMTs are highly correlated and give an absolute resolution limit of 1 part in 10^3 with 1μs resolution. The temporal resolution is ultimately limited by the PMT rise time and the temporal resolution of the oscilloscope and any signal amplifiers. Our ultimate temporal resolution limit is 2 ns, with corresponding sensitivity loss.

There is considerable electrical pick-up from the ionization pulse laser when the Q-switch fires. It is difficult to measure absorption in the first 500 ns against this large background. As result we have not been able to resolve an absorption signal even after averaging over 1000 cycles.

2.2.2 Ion Fluorescence Measurement

We decided to try a slightly different measurement that would be more resilient to electrical pick-up. We measure ion fluorescence scattered from the probe laser beam.
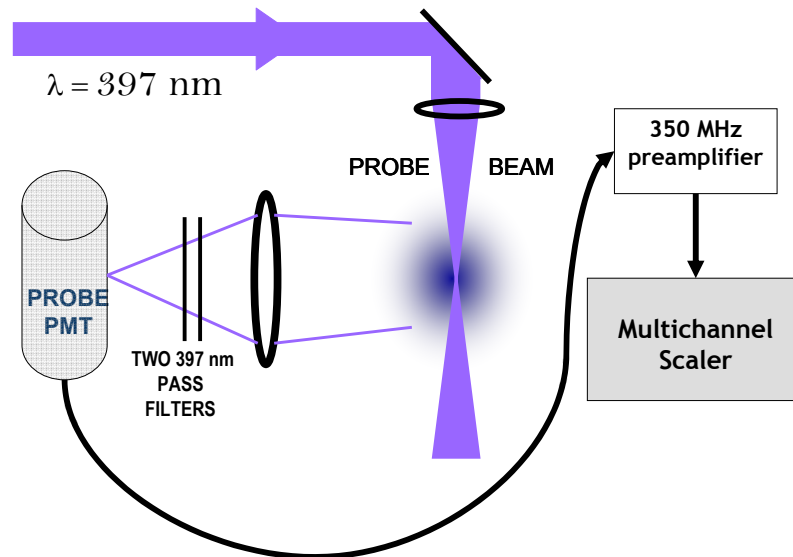
Figure 2.4: Detection of Ion Fluorescence. The probe beam is focused spot 100 μm waist and is absorbed by plasma ions. Ions fluoresce in random directions. Some photons are collected and counted by the Probe PMT.

The plasma fluorescence is focused onto the signal PMT, as shown in Fig. 2.4. Because of the low light levels we use photon counting techniques. We block out room lights and MOT fluorescence with two narrowband-pass filters which together transmit 16% of 397 nm fluorescence and block out all other wavelengths. The electrical signal is amplified and then measured by a multichannel scaler. The scaler allows us to bin the fluorescence signal in time. The bin size is controlled by the scaler and can be as small as 5 ns/bin. The primary benefit of binning is an improved signal-to-noise ratio.

Chapter 3

Ion Imaging Laser

The ion imaging laser has been our greatest challenge. We tried two methods of generating the 397 nm laser: a grating stabilized blue laser diode and a frequency-doubled 794 nm IR laser diode.

3.1 Frequency Doubled IR Laser Diode

In our first experiments we used a robust and economical infrared laser diode and frequency-doubled it to produce a blue 397 nm beam. The IR laser diode with the best spectral properties had low output power, about 5 mW. We amplified this laser beam by injection seeding. The output of our master laser was sent into the powerful laser diode, with 25 mW output power.

We frequency-doubled the 794 nm laser in a BBO-build up cavity. The conversion efficiency in the frequency doubling cavity was 0.1%. Our initial experiments had about 25 μW at 397 nm, of which 20 μW was used for the atom lock and to monitor noise, leaving only 5 μW to probe the plasma. The beam waist at the plasma was 160 μm giving an intensity of 12 mW/cm^2. This is much lower then the saturation

19

intensity, which is 50 mW/cm^2 for this optical transition. With this power we would need a beam waist of 112 μm to achieve saturation.

We also attempted to amplify the IR laser so we would have more blue power. Amplification produced $\sim$ 1 mW of blue laser light. However noise could not be reduced from the lock circuit and we were unable to lock the laser to the 397 nm ion line.

3.2 Blue Laser Diode

We recently invested in a blue diode laser at 397 nm which provides us with 3-5 mW of power. The laser is frequency-narrowed with feedback from a grating so that the spectral output is single frequency and locked to the ion transition.

The laser diode is frequency-narrowed by the Littrow method. A diffraction grating is put in front of the diode laser output. In this setup reflections off the grating follow the Littrow condition: $2d\sin\theta = n\lambda$, where d is the grating groove spacing, θ is the reflection angle, n is the order number, and λ is the laser wavelength. The first-order reflection feeds back to the laser, forcing lasing at that wavelength. The diode laser wavelength is tuned by tilting the grating. The zeroth-order reflection is the laser output.

We have locked the laser diode to the ion transition and attempted imaging the ions. However, no fluorescence signal was observed due, perhaps, to the laser's poor spectral quality. To confirm this we put all the laser power through a plasma discharge cell and looked for a Lamb Dip in the saturated absorption signal (see Sec. 6.1.1). No Lamp dip was observed in the Doppler broadened signal.

20

We recently modified the distance between the grating and the laser diode, which improved scanning and spectral stability at resonance. Hopefully this will improve the spectral quality of the laser beam, allowing us to lock to the ion line and image the ions.

Chapter 4

Results

We probed the plasma ion density by measuring the ion fluorescence due to a 397 nm probe beam. A single oscilloscope trace is shown in Fig. 4.1. The sharp peaks are single photon counts as they strike the PMT - except the first spike which is scattered light from the pulsed laser. The signal can be averaged over many cycles using a multichannel-scalar. The scalar averages and bins the photon counts into a histogram. After subtracting the background we have a signal-to-noise ratio of 10:1 with a bin size of 40 ns/bin. If we bin at 120 ns/bin (Fig. 4.2) the signal-to-noise ratio is 20:1. This signal level is high enough for us to resolve a shock wave. However, a few improvements are in process to enhance our signal.

The lens that collects the fluorescence image only gets a portion of the fluoresced solid angle, which amounts to collecting .16% of the original fluorescence. The 2 narrowband-pass filters (at 397 nm) reduce the signal by another factor of 6.25. Since the quantum efficiency of the PMT is 30% our collection efficiency is 1 photon detected for every 12,800 scattered. However, that is just for one photon recoil. The lifetime of the ion upper state is 7 ns and if we scale Fig. 1.2, pg. 6, for calcium we
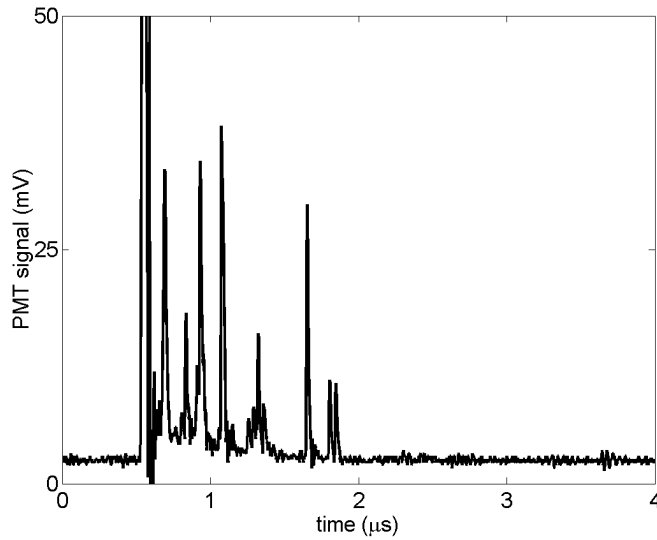
23

Figure 4.1: Calcium ion fluorescence single oscilloscope trace measured by PMT photon counting. The large peak at 0.5 μs is scattered light from the photoionizing pulse.

find the ion velocity to be about 100 m/s. In the absence of optical pumping, with a probe beam waist of 160 microns, 1 ion will scatter 500 photons before leaving the probe beam. So we could measure 1 photon count for every 56 ions in the beam.

The signal in Fig. 4.2 decays after a short period of time. This decay is *not* due to the plasma expanding and ions moving out of the probe beam, but due to optical pumping (see Fig. 4.3). On average the ions cycle between the upper state, $^2P_{1/2}$, and ground state, $^2S_{1/2}$, 17 times before decaying into a dark state, $^2D_{3/2}$, which is a state that doesn't decay back to the ground state quickly. So an ion does not scatter 500 photons while in the probe beam, it only scatters 17 photons and becomes 'dark'.

We have about 1×10^5 ions in the plasma, but only 110 are illuminated and
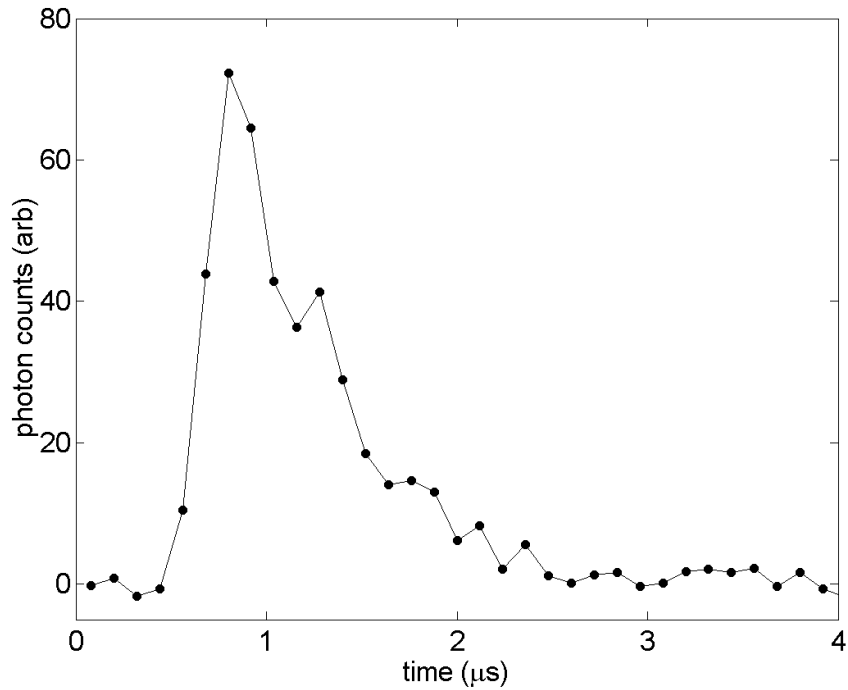
24

Figure 4.2: Calcium ion fluorescence. Averaged over 4000 acquisitions at 120 ns/bin. Background data, also averaged over 4000 acquisitions, has been subtracted. The photoionizing pulse noise has subtracted out nicely.

in resonance with the probe beam[1]. When we consider optical pumping we find that on average only 0.15 photons are collected in each acquisition and in 4000 acquisitions about 600 photons are counted. Our greatest limitation in measuring the ion expansion is the number of ions in resonance with the probe beam.

The number of ions imaged could be improved by increasing the total number of ions, improving the collection efficiency, or reducing optical pumping. We can improve our collection efficiency by a factor of 20 by moving the collecting lens closer to the plasma. Optical pumping can be reduced by adding a repumper, which will

---

[1]The number of ions illuminated and in resonance with the probe beam is a function of the ratio of initial plasma radius to probe beam waist (9.4), and the number of ions in the same Doppler velocity class as the probe beam (estimated to be 10% of all ions).

25

pump the ions from the dark state back into the upper state. This should increase our

fluorescence signal by a factor of a ten and allow detection of the plasma expansion.
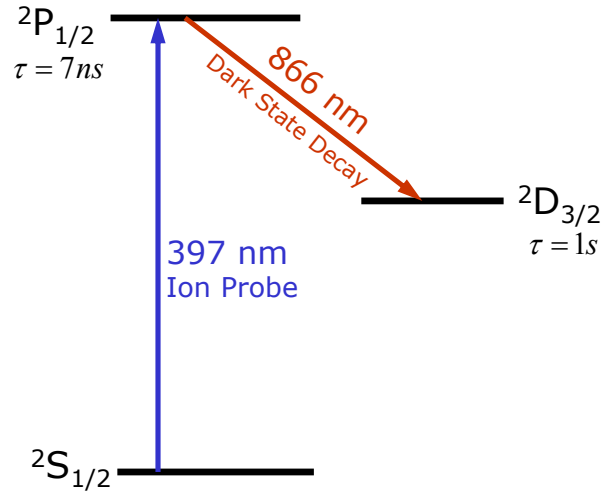

Figure 4.3: Calcium Ion Energy Levels.

We further investigated the effect of dark state decay on the ion fluorescence

signal by solving population rate equations for the three ion states. The results are

shown in figure 4.4, for probe laser power of 5 mW. This graph was also animated

in Maple© for various probe laser powers. For very low laser powers, 1 μW, the

$^2S_{1/2}$ population goes completely to the $^2D_{3/2}$ state at about 0.1 μs. The population

transfer occurs earlier as the laser power is increased. At 3 mW the transfer happens

at $t \approx 100$ ns and there is no further change in transfer time. Laser powers above

3 mW further increase the $^2P_{1/2}$ population at early times ($t < 100$ ns). At 300 mW

half the ions are in the $^2P_{1/2}$ state for $t < 100$ ns. From this calculation we see how

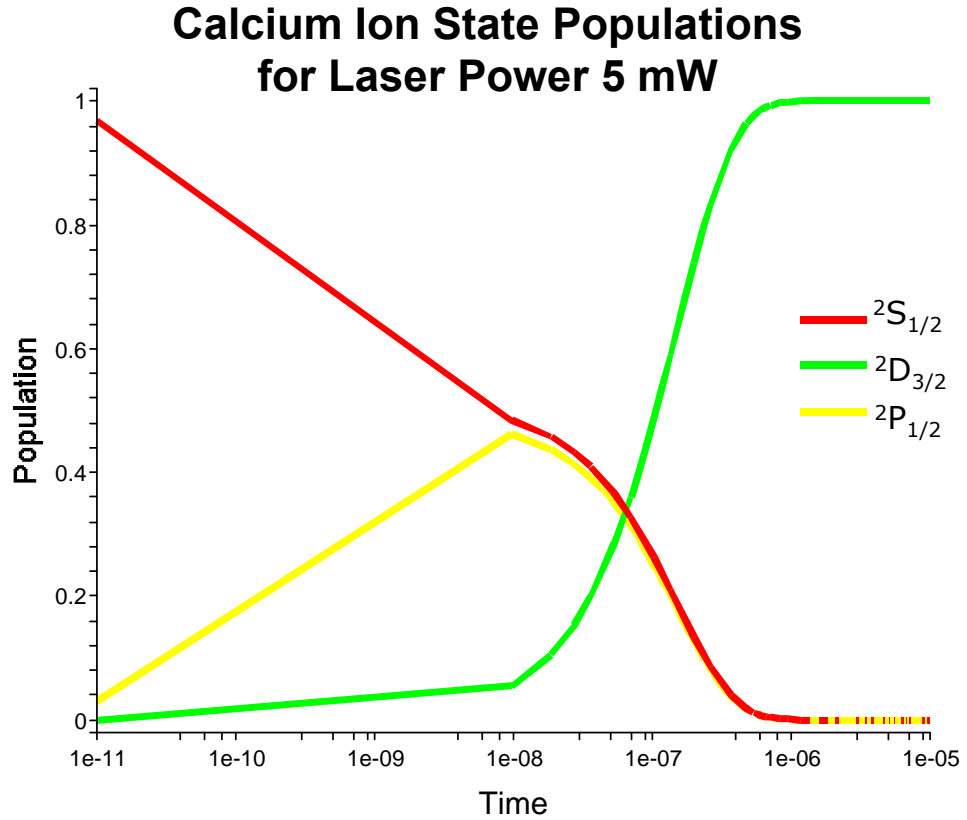vital a repumper is for measuring the ion dynamics.

Figure 4.4: State populations in the calcium ion. Ground $^2S_{1/2}$, upper $^2P_{1/2}$, dark $^2D_{3/2}$.

Chapter 5

Conclusions and Further Work

We have successfully implemented the first fluorescence detection of ions in an expanding ultracold plasma. The fluorescence of a small probe beam is detected by a PMT. This signal is averaged over 4000 acquisitions and has a temporal resolution of 120 ns, limited by the chosen scaler bin size. The greatest limitation of this method is the number of ions, which limits our signal, requiring an excessive number of acquisitions. Obviously with more ions the fluorescence signal will be larger since more photons would be scattered. An ion repumper is also necessary to overcome decay to dark states and measure the ion expansion. This improvement will enhance our ion fluorescence signal by more than a factor of ten. This means we can either reduce the number of acquisitions we average over or increase our temporal resolution (decrease the bin size).

In the near future we plan to measure the density and number of ions in the plasma as a function of position and time using the new probe laser setup. The expansion of the plasma density profile and formation of the shock wave are of particular interest. We are confident that our fine time resolution and high signal-to-noise will

29

enable us to detect a shock wave, and will improve the measurements made previously. We plan to do this by positioning the probe laser beam at the edge of the plasma and measuring the plasma as it expands through the beam. We expect a shock wave based on our numerical simulation [14] (Fig.1.4).

Chapter 6

Other Projects

My thesis work has produced several major developments in our lab. Three new laser diode systems were developed and employed in the experiment. A laser lock scheme, new to our lab, was successfully employed. We trapped calcium atoms in a Far Off Resonance Trap (FORT). We also discovered that our MOT produces charged calcium molecules. The developments of each of these will be described in the following sections.

6.1   Locking Lasers to Atomic Lines

Laser cooling and imaging experiments require the laser wavelength to match the energy level separation in the atom or ion. If the laser drifts off frequency it no loner interacts with atoms. An additional problem occurs if the laser is spectrally broad. In this circumstance the laser's wavelength may be centered at the right wavelength but because of the frequency profile width, there may not be enough power at the right wavelength. A similar problem occurs when the laser lases at more than one wavelength, causing a lack of power at the right wavelength as well as frequency

stability problems. I devoted a great deal of time and effort to narrow laser frequency profiles and lock the lasers to the proper wavelength.

We lock the laser to an atomic line by generating an error signal, which measures the laser detuning from atomic resonance. Figure 6.1 shows an error signal as a function of detuning from resonance. In this example when the laser is above resonance (region II) the signal is positive and the below resonance signal (region I) is negative. When the error signal is zero the laser frequency matches the atomic resonance. In the zero-crossing region the signal is linear and shows the detuning of the laser frequency from resonance. The error signal is fedback to the laser and adjusts the laser frequency so the error signal equals zero.
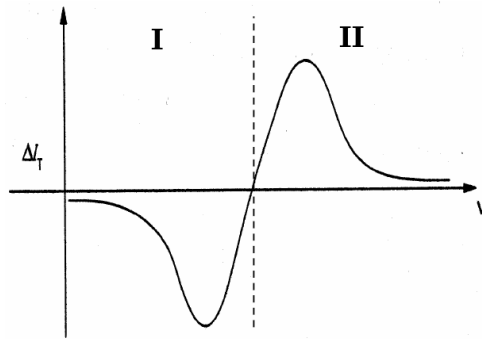
Figure 6.1: Error signal for an atom lock as a function of frequency detuning from atomic resonance. Region I: the laser frequency ν, is below resonance. Region II: ν is above resonance. Error signal is zero when the ν equals the atomic transition.

A number of devices and techniques can be used to generate an error signal. The following sections describe the concepts and techniques used to narrow and lock four of the lasers used in our experiment. Some of our lasers are for calcium atoms,

www.manaraa.com

others are locked to calcium ion transitions. Since the following principles apply to both atom and ion locks for convenience I will refer only to atom locks.

6.1.1 Saturated Absorption

In Saturated Absorption an error signal is generated by saturating the atomic sample. When a laser beam is spectrally scanned across an atomic resonance a Doppler broadened absorption signal, a Maxwellian profile, is measured. When this laser beam is above the saturation intensity, I_{sat}, a large fraction of the atoms are pumped into the upper state. This pump laser beam causes enough excitation that a weaker probe beam counter-propagating the sample, is transmitted through the sample, causing a Lamb dip in the probe beam absorption profile. This occurs when the probe and pump address the same velocity class. The Lamb dip essentially finds the atomic resonance and an error signal can be generated from it.

The pump laser beam must be above the saturation intensity inside the atomic sample to use saturated absorption. The saturation intensity is:

$$I_{sat} = \frac{2\pi^2 hc}{3\lambda^3}\Delta\nu \tag{6.1}$$

where $\Delta\nu$ is the transition linewidth and λ is the transition wavelength. Saturation intensities for the wavelengths we are using are:

423 nm $\longrightarrow$ 60 mW/cm^2

672 nm $\longrightarrow$ 823 μW/cm^2

397 nm $\longrightarrow$ 50 mW/cm^2

866 nm $\longrightarrow$ 4.3 mW/cm^2

33

We generate the error signal by modulating the laser frequency using high frequency RF techniques. Laser RF modulation causes the laser to output three simultaneous frequencies: ω_c the original laser frequency or carrier frequency, and two sidebands $\omega_c - \omega_m$ and $\omega_c + \omega_m$, where ω_m is the modulation frequency. The RF modulation frequency ω_m, is determined by the atomic resonance. For the MOT laser diode $\omega_m = 38$ MHz.

After the laser beam passes through the atomic sample the interference of the sidebands and the carrier is measured. The laser beam intensity is first converted into an electrical signal by a photodiode. The electrical signal contains a beat signal at the RF modulation frequency ω_m. The beat note between the carrier and lower sideband, $\omega_c - \omega_m$, is 180° degrees out of phase with the carrier-high sideband beat note. The beat note between the two sidebands is high frequency and filtered out (low-pass filtered).

When the carrier frequency is above atomic resonance, ω_c and $\omega_c - \omega_m$ create the beat note, and when the carrier frequency is below resonance, ω_c and $\omega_c + \omega_m$ create the beat note. Demodulating the signal transfers the ω_m beat note to a DC signal, containing the beat note's amplitude and phase information. This DC signal is our error signal.

6.1.2 DAVLL

The DAVLL [21], or Dichroic-Atomic-Vapor Laser Lock, produces an error signal by exploiting the Zeeman shift and circularly polarized light. For example, the ground state of calcium is $j = 0$ and the upper state is $j = 1$. In the presence of a magnetic

34

field the $j = 1$, $m = \pm 1$ energy levels shift (see Fig. 6.2). Specific light polarizations excite ground state calcium to specific $^1P_1$ magnetic sub-levels. Specifically, calcium atoms excited to $j = 1$, $m = -1$ absorbed left circularly polarized light, σ^-; while calcium in $j = 1$, $m = +1$ state absorbed right circularly polarized light, σ^+. Atoms excited to the $j = 1$, $m = 0$ state correspond to linearly polarized light, π. The quantization axis is defined by the magnetic field vector $\mathbf{B}$. When the laser beam electric field, $\mathbf{k}$, is parallel to $\mathbf{B}$, the π absorption profile is not observed [22].
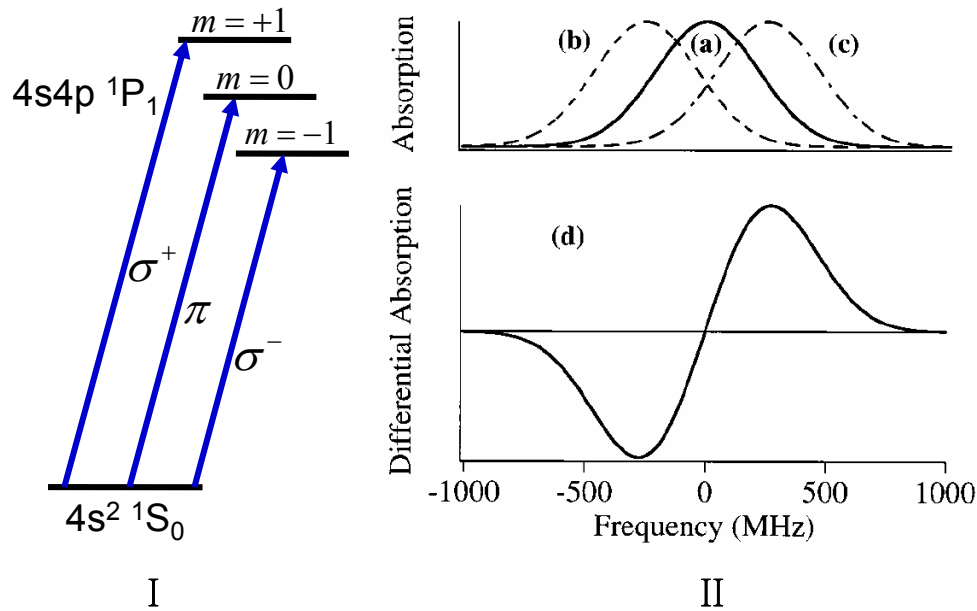

Figure 6.2: Generation of DAVLL Error Signal [21]. I Zeeman shift in calcium. II(a) Absorption profile no magnetic field, or π polarized light in a magnetic field. (b) Absorption profile of σ^- with magnetic field. (c) Absorption profile of σ^+ with magnetic field. (d) Subtraction of (b) and (c), the error signal.

Because the Zeeman shift causes the $m = \pm 1$ to be shifted in energy the σ^- absorption profile shifts down in frequency from the π profile, and the σ^+ shifts up in frequency (see Fig. 6.2). The subtraction of σ^+ and σ^- absorption profiles results in the error signal.

In our DAVLL setup, a magnetic coil surrounds the atomic sample and the laser beam is linearly polarized in the plane orthogonal to $\mathbf{B}$ as it enters the sample. Linearly polarized light is composed of half σ^- and σ^+ polarizations. After passing through the sample the beam passes through a quarter-waveplate, converting σ^- to vertically polarized light and σ^+ to horizontally polarized light. The light strikes a polarizing beam splitter separating the σ^+ and σ^- signals. The two beams are then detected by separate photodiodes. The subtraction of the σ^+ and σ^- signals produces the error signal.

We used the DAVLL to lock three different laser diodes to their atomic/ionic lines. This required three custom built lock circuits and months of time and effort on our part. The lock for the 672 nm laser and 866 nm laser can stay locked for a couple hours, due to the stability of these lasers. The 397 nm laser is more sensitive.

It is difficult to determine if the DAVLL lock point is exactly at atomic line center. If the gain in the photodiode or electronics of an individual σ signal is unequal to the other, the signal will have a false offset. This would cause the error signal to cross zero at the wrong wavelength, shifting the lock point off line center. The lock point could also be off if the polarization optics are not properly aligned.

This problem is easily solved for the 672 nm repumper. After optimizing the optics and adjusting offsets in the photodiodes, we simply lock the laser to the zero

point and then adjust the offset for the largest MOT.

We don't have a convenient secondary check for the 397 nm ion imaging laser, or the 866 nm ion repumper. We have tried to check the lock points by adjusting the setup for saturated absorption. However, we were unable to see any saturated absorption of the 397 nm beam. This suggests possible spectral or other problems with this laser.

6.2 Calcium Dimers

We have observed molecular ions created ion our MOT. We confirmed this by a time of flight measurement (see Fig 6.3). The ratio of the times of flight for calcium ions created by an ionization pulse and MOT created ions was equal to the square-root of two, proving the MOT ions were twice as massive as Ca[1]. Thus, our MOT creates calcium diatomic ions, or dimers.

MOT dimer formation is well documented as a MOT loss mechanism and is studied in a field called photoassociation spectroscopy. Essentially, photoassociation occurs when a MOT photon and two MOT atoms 'collide' and form an ionized dimer. The exact mechanism varies for each atom. For instance, in rubidium (Rb) it is a 2-step process $Rb + Rb + \hbar\omega \rightarrow Rb_2^* + \hbar\omega_2 \rightarrow Rb_2^+ + e$ [18]. Sodium (Na) dimers form through a 3-step process, $\hbar\omega + Na + Na \rightarrow Na_2^* + \hbar\omega_2 \rightarrow Na_2^{**} \rightarrow Na_2^+ + e$ [19].

Figure 6.4 displays possible calcium photoassociation schemes. The lowest energy level is the molecular potential for two ground state atoms. In both the 1st and 2nd scheme atom **A** absorbs a photon from the slower beam. Because the slower is detuned by 133 MHz, atom **A** only absorbs this photon if atom **B** is close enough to
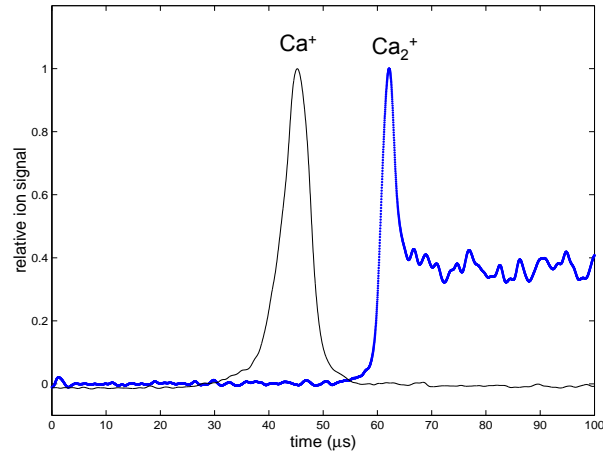
Figure 6.3: Calcium Dimers: The first peak is Calcium ions created by an ionization pulse. The second peak is Calcium dimers created in the MOT.

form the $^1P_1 + {}^1S_0$ molecular potential. This might happen in a three body collision: 1 photon + 2 atoms. In scheme 1 atom **B** absorbs a slower photon and enters an ionized calcium state.

In scheme 2 and 3 photoassociation is proposed to occur from a MOT photon detuned at 38 MHz. We predict in scheme 2 an additional MOT photon excites atom **B**. The pair 'rolls' into the potential dip of the $^1P_1 + {}^1P_1$ state into the calcium dimer potential, casting off an electron as it goes. We tested this theory by shining a spare 423 nm beam into the trap. An AOM (Acoustic-Optical Modulator) further detuned this beam to 20-70 MHz off the atomic line. This detuning is depicted as scheme 3. We could not conclude whether photoassociation caused the formation of our dimers. We were limited in our laser detuning and could not completely study how ion formation depended on a 'pump' laser frequency. To confirm that there is
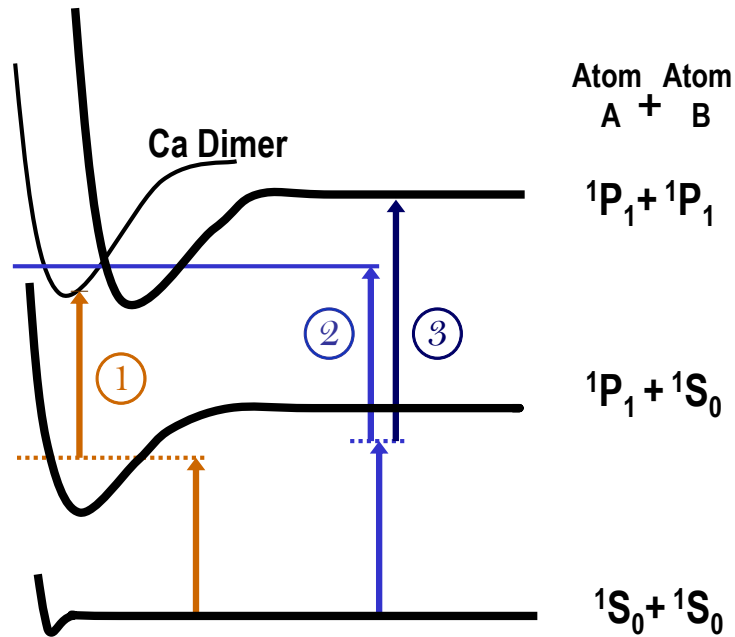
Figure 6.4: Possible calcium dimer formation schemes.

no photoassociation we would need an additional laser to further detune our system from the atomic resonance 423 nm. This is a project for the future.

We also noticed differences in the Ca_2^+ production rate with the applied grid voltage. We did some measurements with the grid voltage at 16 V and 32 V. At 16 V when the atom beam was shut off we saw the ion production shut off immediately and a quadratic decay in optical density. Ions were produced from fast thermal atoms colliding with MOT ions. However, when the grid voltage was raised to 32 volts the ion count did not shut off when the MOT was shut off. Rather the ion count decayed linearly with the optical density. Ions were produced by a completely

different mechanism, independent of thermal beam flux. This seemed very curious to us so we further investigated the grid voltage effect on the dimer formation.
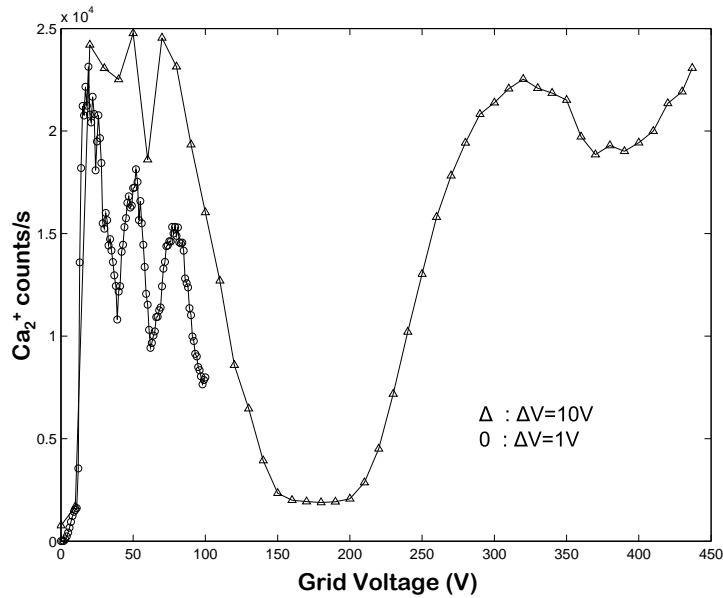

Figure 6.5: Calcium dimer production varies with grid voltage.

We were surprised by what we found as we studied the grids effect on dimer formation. We found a structure in the ion count as the grid voltage was change by few volts. This is not at all what we expected; the grid extraction efficiency is linear with the grid voltage. Unfortunately, we don't have a good explanation for what causes this structure. We are certain it is not due to a Stark shift because the electric field is too weak for a significant shift. We are also certain it isn't caused by liberated electrons colliding, forming more ions which collide and create dimers. There just isn't enough energy in the system for that.

40

6.3 FORT of Calcium Atoms

I also contributed to the trapping calcium atoms in a Far Off-Resonance Trap (FORT), or dipole trap. This work comprises Jared Daily's thesis. I will mention a few details of this work since I contributed to it and presented it at the Optical Society of America conference last October.
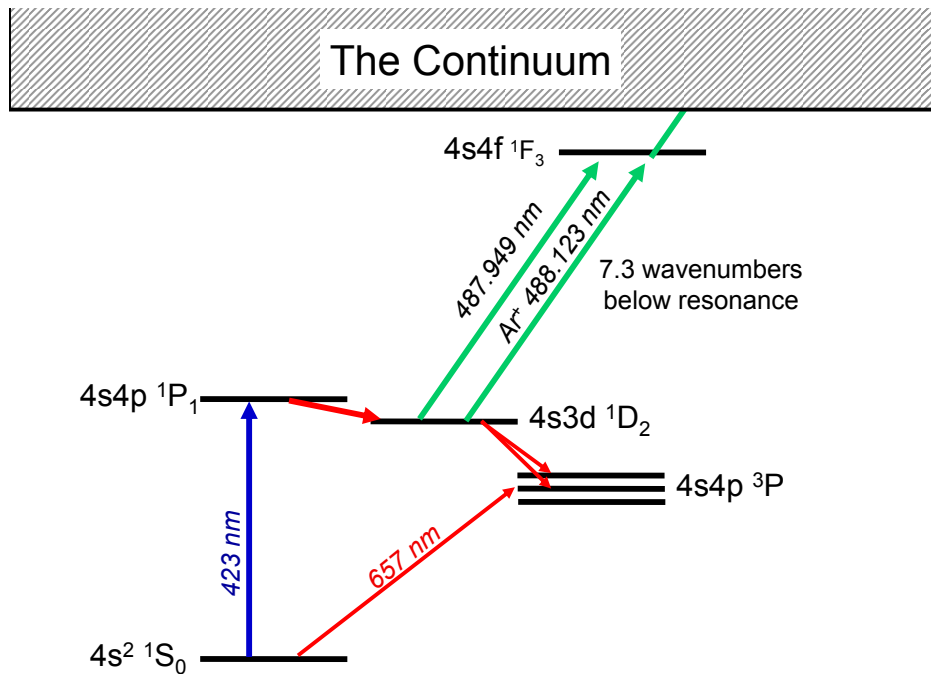

Figure 6.6: Energy Level Scheme for Calcium FORT. Atoms in the $^1D_2$ state are trapped. The argon ion laser $\lambda = 488$ nm excites the atoms and then ionizes from the $^1F_3$ state. These ions are subsequently detected in the channeltron

A FORT traps atoms using the dipole force. Our dipole laser at 488 nm is focused to a Gaussian waist of 20 microns located at the MOT center. The interaction between beam and atom can be described in terms of the AC-Stark shift. The sharp

focus causes an electric field **E** gradient that polarizes the atom. The interaction between these two fields produces a potential, -**P·E**, where **P** is the atom polarization. The rotating wave approximation of this interaction gives an optical potential or 'light shift':

$$U = \frac{\hbar\gamma^2}{8(\omega - \omega_o)}\frac{I(r)}{I_s}, \tag{6.2}$$

where $\gamma = \tau^{-1}$ is the 2π times the natural line width, ω is the laser frequency, ω_o the atomic transition in rad/s, $I(r)$ is the laser beam intensity, and I_s is the saturation intensity of the transition defined in Eq. 6.1. The traps repulsive or attractiveness depends on the dipole laser frequency relative to the atomic transition.

Calcium is a difficult atom to trap in a FORT. A Calcium MOT is relatively hot, ~2 mK, requiring a deep dipole trap potential to over come the atom kinetic energy. Another challenge is competing repulsive and attractive potentials. The MOT trapping line $^1S_0 \rightarrow {}^1P_1$ is not a closed transition. Figure 6.6 shows that atoms in $^1P_1$ also can return to the ground state through the $^1D_2$ and ^3P states. Although the $^1S_0$ ground state is an attractive potential for $\lambda = 532$nm trapping light some other states, particularly $^1P_1$, are quiet repulsive, causing the dipole trap to fail. However, the $^1D_2$ state can be dipole trapped with $\lambda = 488$ nm. It makes a very tight potential for $^1D_2$ atoms, with little Stark shifting of other states. Also, the $^1D_2 \rightarrow 4s4f \; {}^1F_3$ resonance is 220 GHz above the dipole laser frequency, a detuning that enhances the two-photon ionization rate of trapped atoms.

We detect ionized FORT atoms using the channeltron. Figure 6.7 shows the ion count for various dipole laser powers. The ion count number has been normalized

42

by the beam intensity for each data point. If there was no dipole trap the normalized ion count would be the same for all dipole laser powers. The ion count increases with laser power until about 1.5 W. As the power increases beyond ~ 1.5W the ion count begins to drop off. The increased power levels cause Stark shifting of the MOT transition, reducing the MOT population and, subsequently, the number of $^1D_2$ atoms. The dipole trap population is then smaller since there are fewer atoms to trap. An analytical model was iteratively solved generating the curve fit.
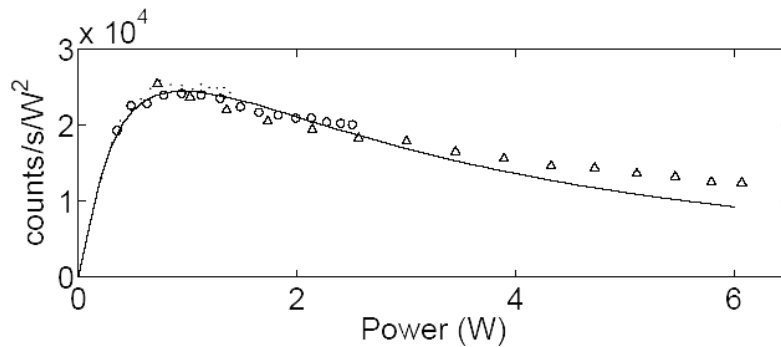

Figure 6.7: Evidence of a $^1D_2$ Calcium FORT. Ion counts verses Dipole laser power. The ion count number has been normalized for the beam intensity.

By measuring the ion production rate at different dipole laser powers we were able to determine the dipole decay rate. The lifetime of the dipole trap is limited by the $^1D_2$ lifetime of ~ 2 ms. We also have strong evidence that the overall trap lifetime

43

is limited to ∼1.5 ms by collisions with the thermal atom beam.

Our initial interest in having a calcium FORT was for our ultracold plasma research. We thought we could load the dipole trap and then create the plasma. This would be advantageous because a FORT has a better defined density distribution and higher density then a MOT. Also since a FORT constrains the calcium in two dimensions, correlation heating will be lower then in the 3-dimensional MOT case. As a result the FORT plasma will be more strongly coupled. In addition, if the plasma contains any low-energy ions they could be trapped in the FORT.

6.4 Papers Published and Presented

The following are papers published or presented during my graduate career at BYU.

Publications

J. E. Daily, R. Gommers, E.A. Cummings, D. S. Durfee, S. D. Bergeson, *Lifetime of the Ca* $4s3d\,^1D_2$ *level measured in an optical dipole trap*, submitted October 2004 to Phys. Rev. A

E.A. Cummings, M. J. Hicken, S. D. Bergeson, *Demonstration of a 1-W injection-locked continuous-wave titanium:sapphire laser*. Applied Optics, **41**, 7583 (2002).

Presentations

Calcium Ion Formation in Optical Traps, Optical Society of America, Rochester, NY, Oct. 2004.

Optical Detection of Ultracold Neutral Calcium Plasmas, Division of Atomic Molecular and Optical Physics, Tucson, AZ, May 2004.

Poster: Absorptive imaging of Ultracold Neutral Calcium Plasmas, American Physical Society Four Corners Meeting, Salt Lake City, UT, Nov 2003.

44

Bibliography

[1] S. Kulin, T.C. Killian, S.D. Bergeson, et al. *Creation of an Ultracold Neutral Plasma*, Phys. Rev. Lett. **83**, 4779 (1999).

[2] S. Kulin, T.C. Killian, S.D. Bergeson, and S. L. Rolston, *Plasma Oscillations and Expansion of an Ultracold Neutral Plasma*, Phys. Rev. Lett. **85**, 318 (2000).

[3] T.C. Killian, et al., *Formation of Rydberg Atoms in an Expanding Ultracold Neutral Plasma*, Phys. Rev. Lett. **86**, 3759, (2001).

[4] T.C. Killian, et al., *Ultracold Neutral Plasmas.* AIP Conf. Proc., **606**, 96 (2002).

[5] T. C. Killian,*Ultracold Neutral Plasmas: Progress and Prospects.* AIP Conf. Proc. **635**, 15 (2002).

[6] C.E.Simien, et al.,*Using absorption Imaging to Study Ion Dynamics in an Ultracold Neutral Plasma.* Phys. Rev. Lett. **92**, 143001 (2004).

[7] T. C. Killian, et al. *Ultracold Neutral Plasmas.* Submitted to Phys. Rev. Lett. Oct. (2004).

[8] F. Robicheaux, James D. Hanson, *Simulation of the Expansion of an Ultracold Neutral Plasma*, Phys. Rev. Lett. **88**, 55002 (2002).

[9] S.G. Kuzmin and T.M. O'Neil, *Numerical simulation of ultracold plasmas*, Phys. Plasmas **9**, 3743 (2002).

[10] S. Mazevet, L.A. Collins, and J.D. Kress, *Evolution of Ultracold Neutral Plasmas* Phys. Rev. Lett. **88**, 2002.

[11] M. S. Murillo, *Using Fermi Statistics to Create Strongly Coupled Ion Plasmas in Atom Traps* Phys. Rev. Lett. **87**, 2001.

[12] J. L. Roberts, Fertig, Lim, S.L. Rolston, *Electron Temperature of Ultracold Plasmas* Phys. Rev. Lett. **92**, 2004.

[13] E. L. Raab, M. Prentiss, Alex Cable, Steven Chu, and D.E. Pritchard, *Trapping of Neutral Sodium Atoms with Radiation Pressure*, Phys. Rev. Lett. **59**, 2631 (1987).

[14] Ross L. Spencer, Brigham Young University, Physics and Astronomy Department (2003). Unpublished.

[15] Harold J. Metcalf and Peter van der Straten. *Laser Cooling and Trapping.* Springer, New York, 1999.

[16] Schmidt, *Physics of High Temperature Plasmas*, Academic Press, New York, 1979.

[17] Ch. Sack and H. Schamel, Phys. Rep. **156**, 311 (1987).

[18] D. Leonhardt and J. Weiner, *Direct two-color photoassociative ionization in a rubidium magneto-optic trap*, Phys. Rev. A. **52**, 1419 (1995).

[19] P. S. Julienne and R. Heather, *Laser Modification of Ultracold Atomic Collisions: Theory*, Phys. Rev. Lett. **67**, 2135 (1991).

[20] S. D. Bergeson, R. L. Spencer, *Neutral-plasma Oscillations at Zero Temperature*, Phys. Rev. E. **67**, 026414 (2003).

[21] K. L. Corwin, et al., *Frequency-stabilized diode laser with the Zeeman shift in an atomic vapor*, App. Optics **37**, 3295 (1998).

[22] B. H. Bransden and C. J. Joachain, *Physics of Atoms and Molecules*, Prentice Hall, New York, 2003.